Supporting Information

Transformative Two-Dimensional Array Configurations by Geometrical Shape-Shifting Protein Microstructures:

Chee Leng Lay,[§, †,‡] *Mian Rong Lee,*[§,‡] *Hiang Kwee Lee,*[§, †] *In Yee Phang,*[†] *Xing Yi Ling*[§,*]

[§]Division of Chemistry and Biological Chemistry, School of Physical and Mathematical Sciences, Nanyang Technological University, Singapore 637371, and [†]Institute of Materials Research and Engineering, Agency for Science, Technology and Research (A*STAR), 3 Research Link, Singapore 117602.

‡These authors contributed equally to this work.

* To whom correspondence should be addressed. Email: xyling@ntu.edu.sg

Supporting Figures

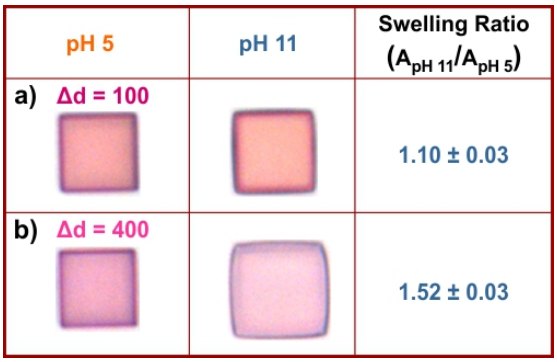

Figure S1. Swelling ratio at different z-layer distance. Optical microscopic images illustrating the area swelling ratio of square BSA micostructures fabricated using a z-layer distance (Δd) of (**a**) 100 nm and (**b**) 400 nm, respectively. Area swelling ratio is calculated by dividing area at pH 11 ($A_{pH\ 11}$) with the area at pH 5 ($A_{pH\ 5}$).

The swelling ability of BSA microstructures is determined by their cross-linking density. Lower cross-linked structures generally exhibit higher swelling ability due to greater freedom of cross-linked network expansion. We can precisely modulate the cross-linking density of BSA microstructures by tuning the fabricating z-layer distance (Δd) during the two-photon layer-by-layer polymerization process, since Δd is inversely proportional to the cross-linking density.[1] Both the BSA microstructures, fabricated using z-layer distance (Δd) of 100 nm and 400 nm, undergo swelling (Figure S1) when the surrounding pH is changed from 5 to 11 due to the presence of BSA protein. With an isoelectric point between pH 4.7 - 4.9, BSA is significantly more negatively charged at pH 11 than at pH 5.[2] Therefore, the BSA microstructure is able to absorb more water through the formation of multiple ion-dipole interactions upon increase in pH, which causes its swelling.[3]

As expected, BSA segments with high cross-linking density (Δd = 100 nm) also demonstrate negligible swelling with a swelling ratio of (1.10 ± 0.03; Figure S1a). On the other hand, BSA segments with lower cross linking density (Δd = 400 nm) has a swelling ratio of (1.52 ± 0.03; Figure S1b), which is ~ 38 % higher than that at Δd = 100 nm. Hence, it is evident that the precise modulation of cross-linking density of a BSA matrix is able to create distinct swelling properties, which forms the basis of our latter design on dynamic geometrical shape-shifting BSA microstructures. Hereby, BSA segments fabricated with z-layer distance of 100 nm and 400 nm will be termed as “skeletal frames” and “responsive BSA matrix”, respectively.

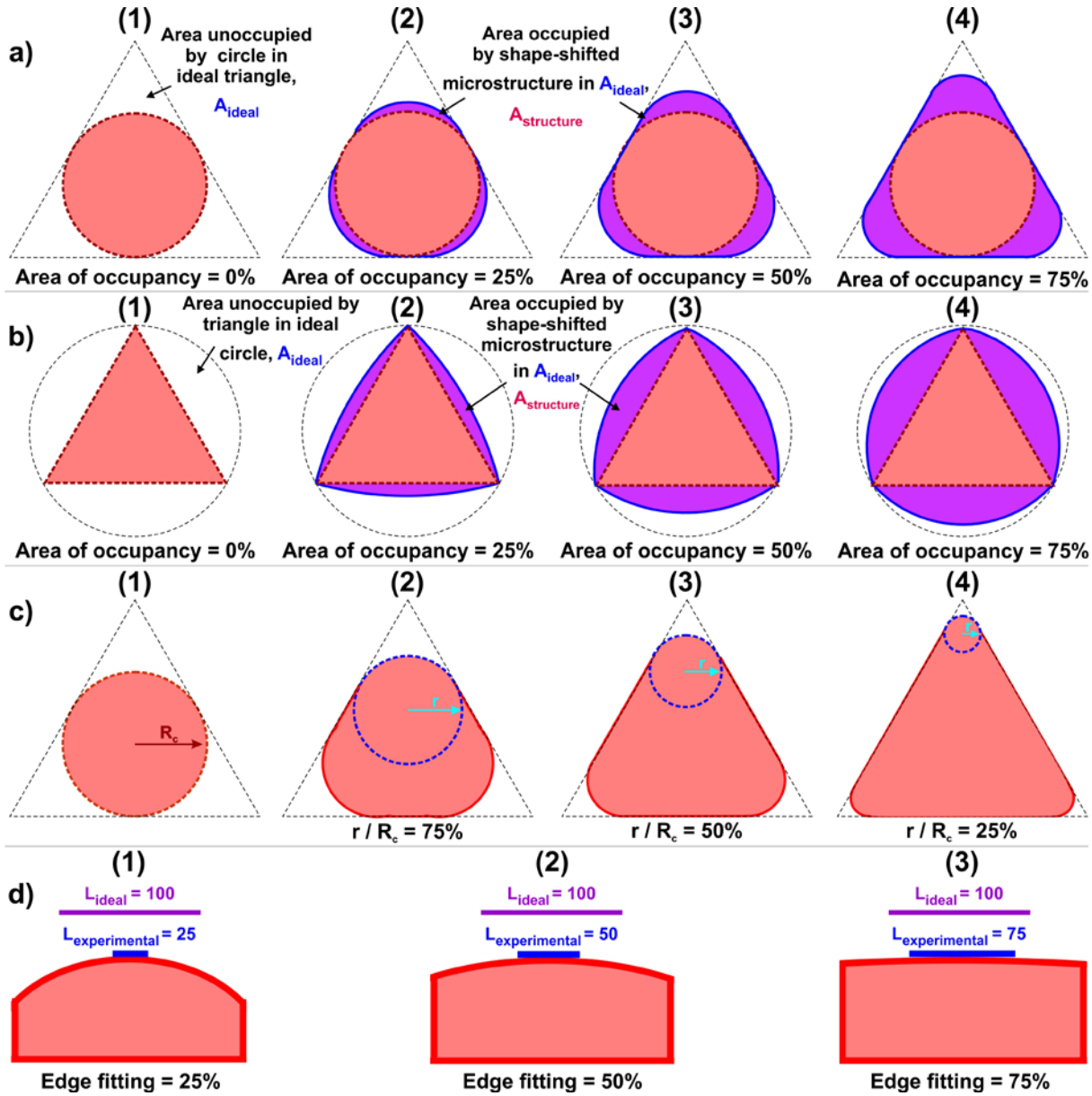

Figure S2. Defining shape-shifting efficacy. (**a – b**) Schematics illustrating the area of occupancy of BSA microstructures (outline in blue) in an ideal shape (outline in black) when it undergo anisotropic swelling to cover (**1**) 0%, (**2**) 25%, (**3**) 50%, and (**4**) 75% of the initial empty area, for circle-to-polygon and polygon-to-circle shape-shifting, respectively. Area of occupancy (area of occupancy = $A_{structure}/A_{ideal}$ x 100%) is obtained by comparing area occupied by shape-shifted BSA microstructure at pH 11 ($A_{structure}$, shaded in blue) with initial empty area of ideal shape (A_{ideal}; Figure S2a(1); Figure S2b(1)). (**c**) Schematic representations of shape-shifted triangular BSA microstructures with protrusion index (protrusion index = r/R_c x 100%) of (**2**) 75%, (**3**) 50% and (**4**) 25%, respectively. "*r*" is the radius of circles (outline in blue) that can be fitted into the protrusions

and (**1**) R_c is the reference radius of curvature at pH 11 of an isotropically swelled circular structure in the absence of skeletal frames (refer to Figure S7e; R_c = 12.2 μm; Δd = 400 nm; swelling ratio ~ 1.5). (**d**) Schematics illustrating the contours of BSA microstructures with edge fitting of (**1**) 25%, (**2**) 50%, and (**3**) 75%, to a hypothetical reference line (purple line). Edge fitting (edge fitting = $L_{\text{experimental}}/L_{\text{ideal}}$ x 100%) is determined by comparing the length of experimental and ideal edges.

To define the overall efficiency of geometrical shape-shifting, we examine the area, radius of curvature and tangent length at edges of final transformed shapes after swelling in comparison to their respective ideal shapes.

Area of occupancy is calculated by dividing the area of protrusions generated by experimentally shape-shifted microstructures ($A_{\text{structure}}$) over area of ideal shape that is unoccupied by the isotropically-swelled microstructure (A_{ideal}) (Figure S2a and 2b). The larger the area of occupancy (area of occupancy = $A_{\text{structure}}/A_{\text{ideal}}$ x 100%), the better a microstructure conforms to its ideal shape and has more well-defined geometrical transition. For a successful shape-shifting event, area of occupancy must be >50%.

To clearly distinguish between a corner and an arc, we measure radius of curvature (RoC) of protrusions generated between adjacent skeletal frames upon shape-shifting of the microstructures at pH 11 (Figure S2c),[4, 5] where a smaller "*r*" denotes a sharper protrusion, and vice-versa. We compare "*r*" to a reference RoC obtained from an isotropically swelled circular microstructure without embedded skeletal frames (R_c) (Figure S2c(1)). A protrusion is defined as a "corner" when the protrusion index (protrusion index = (r/R_c) ≤50%). That is, a protrusion approximates to a corner when it has at least 50% smaller radius of curvature as compared to that of an isotropically swelled ideal circular microstructure (Figure S2c(3–4)). On the other hand, protrusions with protrusion index >50% are classified as "arcs" (Figure S2c).

On the other hand, formation of an edge upon circle-to-polygon transition is classified by edge fitting (edge fitting = $L_{\text{experimental}}/L_{\text{ideal}}$ x 100%) through comparing the percentage of experimental and ideal edge lengths that are in contact at pH 11. An ideal edge line is the longest possible straight

line that can be fitted along the BSA microstructures, whereas experimental edge lines denote regions of the microstructures that are in contact with the ideal edge line (Figure S2d). Contours of microstructures with edge fitting <50% are more rounded and have less regions in contact with the ideal straight line (Figure S2d(1)). When edge fitting >50%, microstructures have flatter contours and have more regions in contact with the ideal straight line (Figure S2d(2–3)). This indicates that the higher the extent of edge fitting, the greater the BSA contour approximate towards a straight line. Hence, we define the "side" of a transformed polygon as an edge only if edge fitting >50%.

Overall, for circle-to-polygon shape-shifting with distinct arc-to-corner/edge transformation, the newly formed polygons should have (1) high conformity to the ideal polygon shapes with area of occupancy >50%, (2) distinct corners with protrusion index ≤50%, and (3) edge fitting >50%. On the other hand, well-defined polygon-to-circle transformations are characterized by (1) high conformity to the ideal circular shapes with area of occupancy >50%, and also (2) distinct arcs with protrusion index >50%.

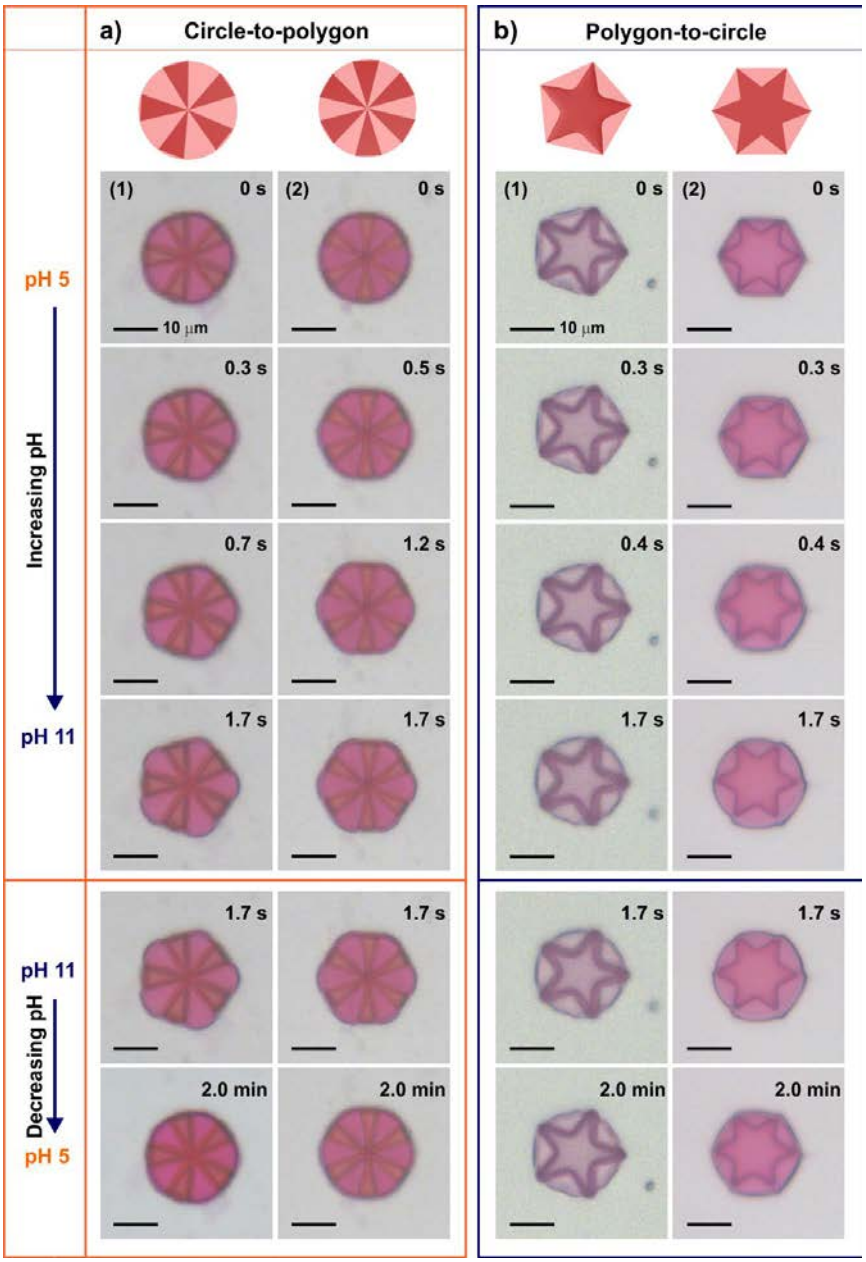

Figure S3. Dynamic geometrical shape-shifting of BSA microstructures. (**a**) Representative movie frames demonstrating the dynamic and rapid circle-to-polygon transformation when pH 5 increases to pH 11 (top), and also the reversed polygon-to-circle shape-shifting (bottom) when pH 11 returns to the initial pH 5. (**b**) Representative movie frames demonstrating the dynamic and rapid polygon-to-circle transformation when pH 5 increases to pH 11 (top), and also the reversed circle-to-polygon shape-shifting (bottom) when pH 11 returns to the initial pH 5. (**1**) Pentagon-to-circle and circle-to-pentagon transformations for (**a**) and (**b**), respectively. (**2**) Hexagon-to-circle and circle-to-hexagon transformations for (**a**) and (**b**), respectively.

Different skeletal frame shapes	Area of occupancy, $A_{structure}/A_{ideal}$ (%)	Protrusion index, r / R_c (%)	Edge fitting, $L_{experimental}/L_{ideal}$ (%)
pH 5 pH 11 a) Triangular 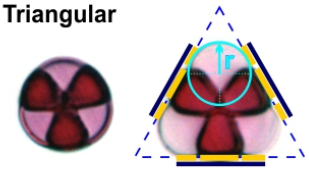	59 ± 2	50 ± 1	87 ± 4
b) Stick-shaped rectangular 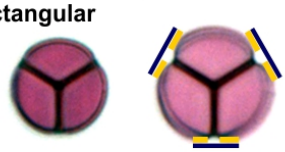	40 ± 2	84 ± 4	70 ± 8
c) Block-shaped rectangular 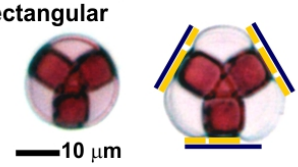 10 μm	40 ± 2	69 ± 3	86 ± 6

Figure S4. Comparison of skeletal frame designs for circle-to-polygon shape-shifting. Evaluation of area of occupancy, protrusion index and edge fitting of shape-shifted BSA microstructures embedded with three equally distributed (**a**) triangle-, (**b**) stick- and (**c**) block-shaped skeletal frames. The measurements highlighted in red denote the parameters that do not fulfill the requirement of circle-to-triangle shape-shifting.

We systematically investigate the effect of skeletal frame's shapes (triangle, stick and block) on circle-to-polygon transformations. BSA microstructures embedded with triangle-shaped skeletal frames exhibit well-defined circle-to-triangle shape-shifting with area of occupancy, protrusion index, and edge fitting of (59 ± 2) %, (50 ± 1) %, and (87 ± 4) %, respectively, which meet all pre-defined criteria (Figure S4a). On the other hand, BSA microstructures embedded with stick-shaped skeletal frames demonstrate area of occupancy, protrusion index, and edge fitting of (40 ± 1) %, (84 ± 4) %, and (70 ± 8) % (Figure S4b), respectively. For block-shaped skeletal frames, the parameters are quantified accordingly at (40 ± 1) %, (69 ± 3) %, and (86 ± 6) % (Figure S4c). Hence, the swelling behavior of both stick-shaped and block-shaped skeletal frames did not meet all the pre-defined criteria, and therefore, cannot be considered as successful and well-defined circle-to-triangle transformations. This highlights the superiority of triangle-shaped skeletal frames over skeletal frames of other shapes to effect well-defined circle-to-triangle shape-shifting. This is due to the sharper parabolic swelling profile generated between adjacent triangle-shaped skeletal frames which create protrusions that are more oblique and sharper.

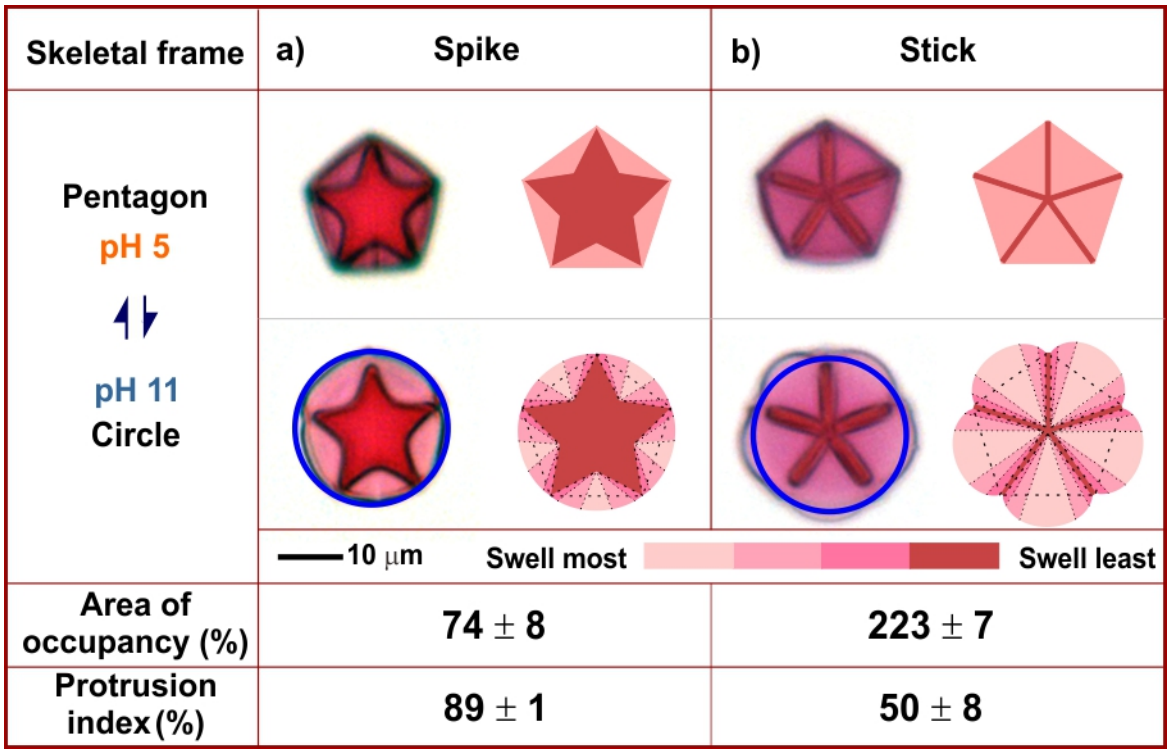

Figure S5. Comparison of skeletal frame designs for polygon-to-circle shape-shifting. Polygon-to-circle shape-shifting of BSA microstructures embedded with (**a**) spike- and (**b**) stick-shaped skeletal frames. Optical images (left) and schematic diagrams (right) illustrating the gradient swelling profile of each BSA microstructure. Ideal circular shapes are outlined in blue over respective transformed BSA microstructures at pH 11.

To compare the effect of frame shape on the distinctness of polygon-to-circle shape-shifting, we embed sharp-tipped spike-shaped skeletal frames (Figure S5a) and blunt-tipped stick-shaped skeletal frames (Figure S5b) into a low cross-linked pentagon microstructure. Pentagon microstructure embedded with spike-shaped skeletal frames transforms into near-perfect circle at pH 11 (area of occupancy = (74 ± 8) %, protrusion index = (89 ± 1) %; Figure S5a). On the other hand, the microstructure embedded with stick-shaped skeletal frames swell to form a contorted circle with area of occupancy and protrusion index of (223 ± 7) % and (50 ± 8) % (Figure S5b), respectively. We would like to highlight that stick-shaped skeletal frames lead to an area of occupancy which is > 2-fold larger than A_{ideal}, denoting the presence of large deviation between the swelled microstructure

and the ideal circle which therefore cannot be considered a well-defined polygon-to-circle transformation.

The well-defined polygon-to-circle transformation contributed by spike-shaped skeletal frames is due to the precise attachment of their sharp tips to the corners of pentagon microstructure (Figure S5a). At pH 11, the pentagon microstructure with spike-shaped skeletal frames embedded swells anisotropically to produce a circle. This defined anisotropic swelling is due to the pinning of the skeletal frames to the five corners of the pentagon which restrict swelling at/near the corners. As a result, a broad arch-shaped swelling profile occurs along all the edges of the pentagon to form arcs (protrusion index = (89 ± 1) %) which leads to the pentagon-to-circle transformation.

However, the blunt tips of the stick-shaped skeletal frames are not well attached to the corners of the pentagon microstructure. At pH 11, the pentagon microstructure also undergoes anisotropic swelling, but to form a contorted circle instead. The contorted circle exhibits much sharper protrusions (protrusion index = (50 ± 8) %) and has area extended beyond its ideal circular shape (area of occupancy = (223 ± 7) %; Figure S5b). These observations clearly demonstrate that the sharp, spike-shaped skeletal frame is essential to bind and restrict swelling near the corners effectively for the generation of well-defined arcs (protrusion index = (89 ± 1) %) in polygon-to-circle transformation. This is superior to blunt, stick-shaped skeletal frames, which are poorly attached to the polygon's corners and hence do not promote distinct polygon-to-circle shape-shifting.

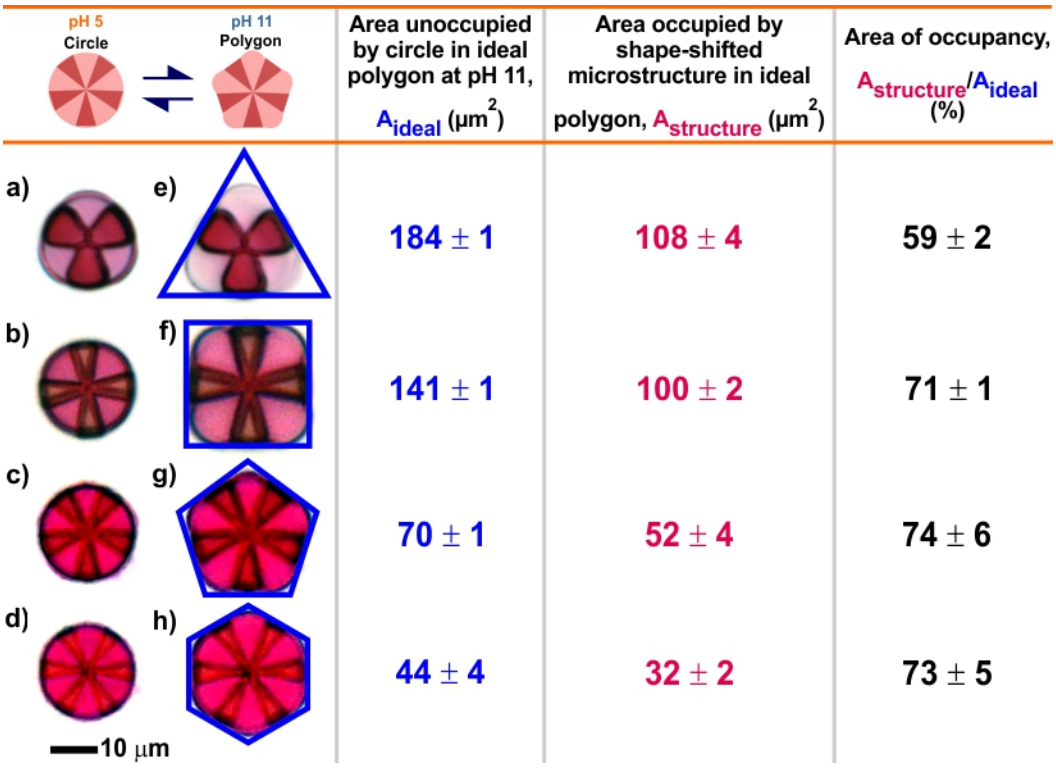

Figure S6. Area of occupancy of circle-to-polygon shape-shifting microstructures. Schematic representations (top) and optical microscopic images (bottom) of dynamic geometrical shape-shifting of circular BSA microstructures (**a** - **d**) at pH 5 to (**e**) triangle, (**f**) square, (**g**) pentagon, and (**h**) hexagon at pH 11. Ideal shapes of polygons (**e** – **h**) are outlined in blue over respective transformed BSA microstructures at pH 11. A successful shape-shifting event occurs only when the area of occupancy ($A_{structure}/A_{ideal}$ × 100%) of shape-shifted BSA microstructure is >50% upon pH stimulation.

Using the concept of area of occupancy ($A_{structure}/A_{ideal}$ × 100%), our circle-to-polygon BSA microstructures are subsequently evaluated to determine the effectiveness of their geometrical shape-shifting. We quantify the experimental area of occupancies at 59%, 71%, 74% and 73% for the shape-shifting of initial circular BSA microstructure to triangle, square, pentagon and hexagon (Figure S6), respectively. Notably, all the circle-to-polygon shape-shifting BSA microstructures exhibit an area of occupancy of >50%, which clearly indicates that the transformed microstructures approximate closely to their respective ideal shapes as a result of well-defined circle-to-polygon transitions.

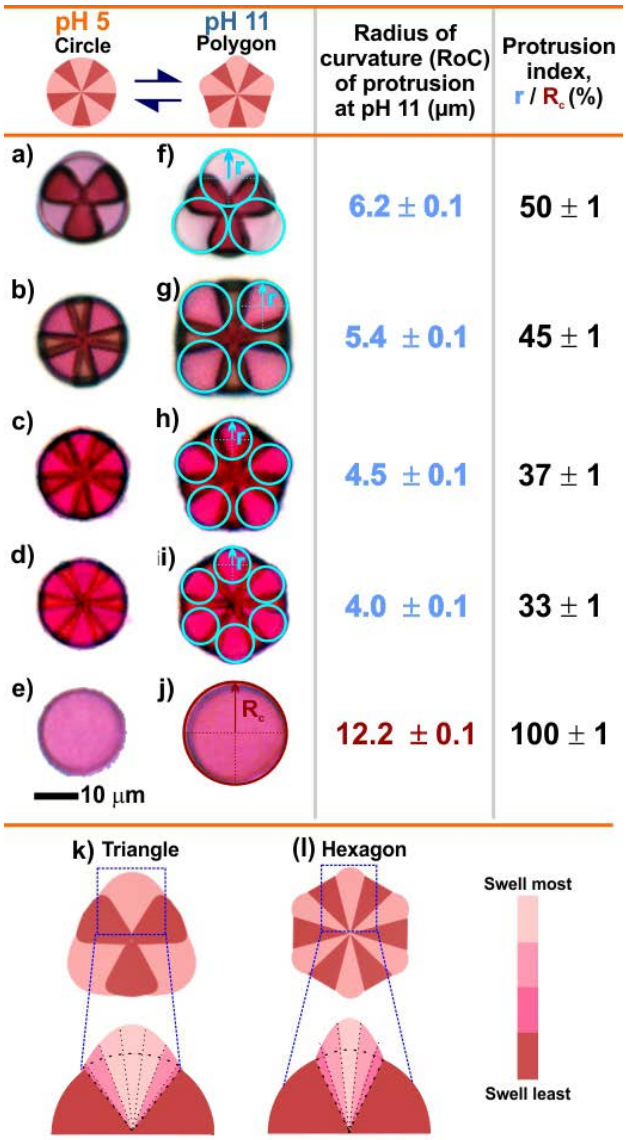

Figure S7. Protrusion index of circle-to-polygon shape-shifting microstructures. Schematic representations (top) and optical microscopic images (bottom) of dynamic geometrical shape-shifting of circular BSA microstructures (**a** - **d**) at pH 5 to (**f**) triangle, (**g**) square, (**h**) pentagon, and (**i**) hexagon at pH 11. Ideal circles (cyan) are fitted into generated protrusions of respective polygons at pH 11 to determine their radius of curvature (*r*). (**e**, **j**) Optical microscopic images of circular BSA microstructure (z-layer distance, Δd = 400 nm) without skeletal frame at pH 5 and pH 11, respectively. The control circular BSA microstructure undergoes isotropic swelling (swelling ratio ~ 1.5) at pH 11 and has a radius of curvature (R_c, red) of 12.2 μm. (**k**, **l**) Schematic illustrations of the anisotropic swelling for circle-to-triangle and circle-to-hexagon shape-shifting, respectively.

The radius of curvature (RoC), and therefore the protrusion index, of all the shape-shifted BSA microstructures are quantified to distinguish between arc and corner for circle-to-polygon transformations. This is one of the determining factors for achieving well-defined geometrical shape-shifting. We observe that the protrusion index for the shape-shifted triangle, square, pentagon and hexagon are 50%, 45%, 37% and 33%, respectively (Figure S7). The general protrusion index of ≤50% therefore indicate that protrusions generated on swelling at pH 11 can be identified as corners, clearly exemplifying the arc-to-corner transition which is crucial for circle-to-polygon transformation.

Furthermore, the newly-generated corners generally become sharper as the number of skeletal frames embedded increases from three (triangle; protrusion index ~ 50%) to six (hexagon; protrusion index ~ 33%). For the circle-to-triangle transformation, the relatively higher protrusion index can be attributed to the larger separation distance of adjacent skeletal frames. Regions of responsive BSA matrix attached to or near the skeletal frame experience a greater resistance to swell (lower swelling ratio) as imposed by the stationary skeletal frame (Figure S7k). On the other hand, regions of the same BSA segments further away from skeletal frames are less constrained and exhibit greater swelling ability.[6] Consequently, the larger separation of adjacent skeletal frames in a circle-to-triangle shape-shifting microstructure creates broad parabolic swelling profiles which result in the formation of truncated corners with protrusion index ~ 50%. In contrast, the close proximity of adjacent skeletal frames, such as in circle-to-hexagon BSA microstructures, leads to a sharper swelling profiles which generate well-defined corners with a smaller protrusion index of ~ 33% (Figure S7l). The importance of skeletal frame in directing anisotropic swelling for geometrical shape-shifting is again emphasized when a control circular microstructure (Figure S7j), in the absence of skeletal frame, undergoes an isotropic swelling without geometrical shape change.

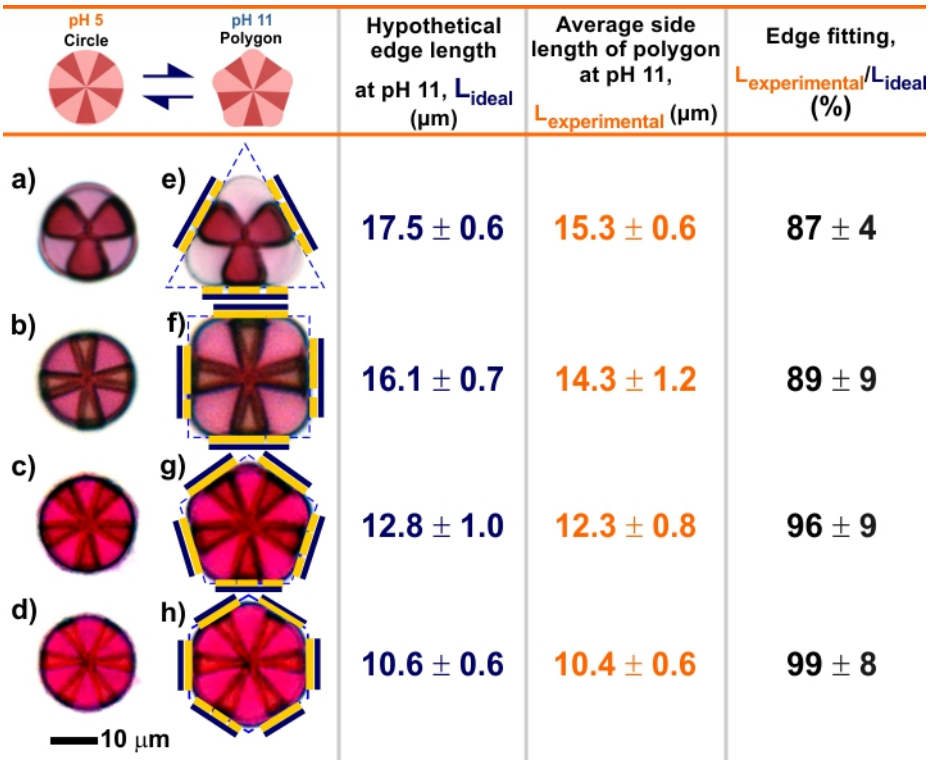

Figure S8. Edge fitting of circle-to-polygon shape-shifting microstructures. Schematic representations (top) and optical microscopic images (bottom) of dynamic geometrical shape-shifting of circular BSA microstructures (**a** - **d**) at pH 5 to (**e**) triangle, (**f**) square, (**g**) pentagon, and (**h**) hexagon at pH 11. Shapes of respective ideal polygons are outlined with blue dotted lines. Tangent lines on each side of transformed polygons (side length, $L_{experimental}$) are outlined in orange and ideal edge lengths (L_{ideal}) are in black. Edge fitting ($L_{experimental}/L_{ideal} \times 100$ %) is determined by comparing the length of experimental and ideal edges.

Based on our experimental results (Figure S8), all the sides of our transformed polygons, including triangle, square, pentagon and hexagon, are considered as edges due to their large similarities as a straight line (edge fitting >50%), which is the basis for the definition of an edge.

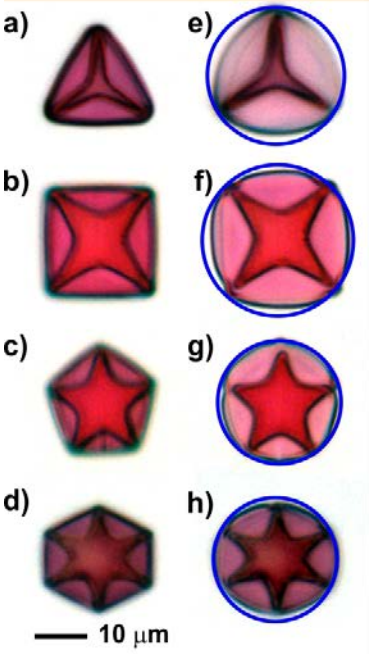

Area unoccupied by polygon in ideal circle at pH 11, A_{ideal} (μm^2)	Area occupied by shape-shifted microstructure in ideal circle, $A_{structure}$ (μm^2)	Area of occupancy, $A_{structure}/A_{ideal}$ (%)
304 ± 4	231 ± 6	76 ± 3
235 ± 2	173 ± 5	74 ± 3
100 ± 2	74 ± 7	74 ± 8
71 ± 1	50 ± 6	70 ± 8

Figure S9. Area of occupancy of polygon-to-circle shape-shifting microstructures. Schematic representations (top) and optical microscopic images (bottom) of dynamic geometrical shape-shifting BSA microstructures from (**a**) triangle, (**b**) square, (**c**) pentagon, and **(d**) hexagon at pH 5 to circular shapes (**e** - **h**) at pH 11. Ideal shapes of circle (**e** - **h**) are outlined in blue over respective transformed BSA microstructures at pH 11. A successful shape-shifting event occurs only when the area of occupancy ($A_{structure}/A_{ideal}$ × 100%) of shape-shifted BSA microstructure is >50% upon pH stimulation.

For polygon-to-circle (triangle, square, pentagon and hexagon) shape-shifting, we observe that all our microstructures demonstrate well-defined geometrical transformations where area of occupancy is >50% for all the microstructures (Figure S9).

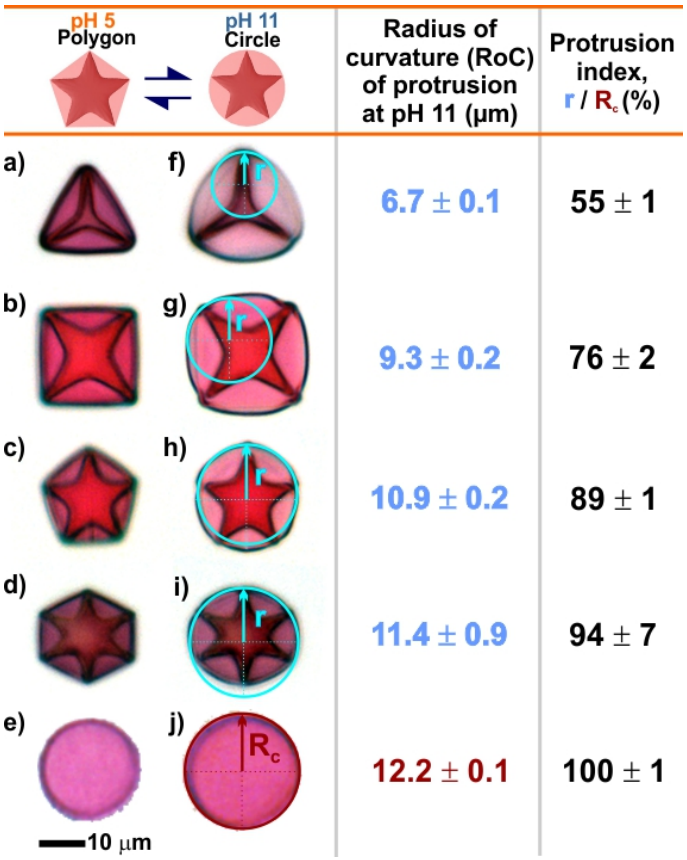

Figure S10. Protrusion index of polygon-to-circle shape-shifting microstructures. Schematic representations (top) and optical microscopic images (bottom) of dynamic geometrical shape-shifting BSA microstructures from (**a**) triangle, (**b**) square, (**c**) pentagon, and (**d**) hexagon at pH 5 to circular shapes (**f** - **i**) at pH 11. Ideal circles (cyan) are fitted into corners of the respective transformed BSA microstructures to determine their radius of curvature (*r*). (**e**, **j**) Optical microscopic images of circular BSA microstructure (z-layer distance, Δd = 400 nm) without skeletal frame at pH 5 and pH 11, respectively. The control circular BSA microstructure undergoes isotropic swelling (swelling ratio ~ 1.5) at pH 11 and has a radius of curvature (R_c, red) of 12.2 μm.

By measuring the RoC of transformed BSA microstructures in regions near the skeletal frames, we determine the protrusion indexes for the shape-shifted circles from triangle, square, pentagon and hexagon at 55%, 76%, 89% and 94% (Figure S10), respectively. Our results therefore demonstrate that all our BSA microstructures have undergone corner-to-arc conversion to effect polygon-to-circle transformations upon exposure to pH 11, as the criteria of arc classification (protrusion index >50%) has been fulfilled.

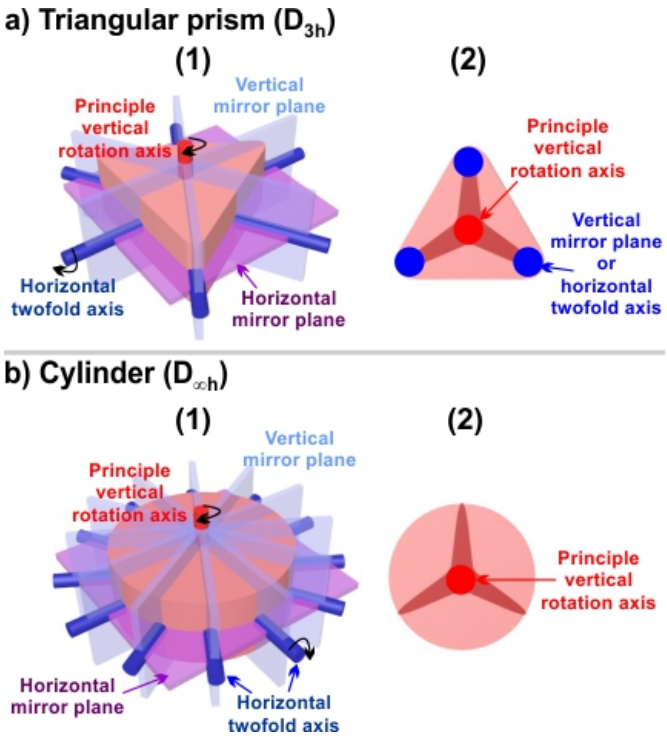

Figure S11. Point-group symmetry and "nodes" allocation. Symmetrical geometric figures of (**a**) triangular prism (D_{3h}) and (**b**) cylinder ($D_{\infty h}$) are used to describe the point group symmetry of triangular BSA microstructure and shape-shifted circular microstructure, respectively. (**1**) Schematic illustrations of three-dimensional geometric figures of the respective point groups described in Schoenflies symbols. (**2**) Schemes depicting the assignment of "nodes" in the respective BSA microstructures to represent their point group symmetry.

To differentiate the array configurations upon geometrical shape-shifting at pH 11, we assign "nodes" to both triangular and shape-shifted circular BSA microstructures according to their point-group symmetry.[7-10] The initial as-fabricated triangular BSA microstructure has a point group (D_{3h}) similar to a triangular prism, as characterized by its 3-fold vertical rotation axis, three horizontal 2-fold axes, three vertical vertex-to-edge centre mirror planes and one horizontal mirror plane (Figure S11a(1)).[8, 9] Consequently, the point group symmetry of our triangular BSA microstructure can be reflected using a simpler "nodes" representation, where these "nodes" are allocated on the vertices and centre of microstructure to accurately denote its D_{3h} symmetry (Figure S11a(2)). Although the assignment of "nodes" only at the vertices of triangular microstructure also leads to a similar D_{3h}

symmetry, we emphasize that the allocation of a “node” at the centre is crucial to describe the position of the microstructure, which we acknowledge remain unchanged throughout the pH stimulation. The centre “node” serves as a basis of comparison with other array configurations while preserving the D_{3h} symmetry of triangular microstructure, and also exemplifies the importance of geometrical shape-shifting to effect topographical change in array configurations. In other words, we aim to achieve and clearly illustrate transformations of 2D array configurations by acknowledging the change in number of reference “nodes” in a single microstructure upon geometrical shape-shifting, even without re-positioning the as-fabricated microstructures.

On the other hand, circular BSA microstructure adopts cylinder’s point group $D_{\infty h}$ which has infinite rotational symmetry, infinite vertical mirror planes and 1 horizontal mirror plane (Figure S11b(1)).[7, 10] Such $D_{\infty h}$ symmetry can be in turn represented by assigning only 1 “node” to the centre of shape-shifted circular BSA microstructure (Figure S11b(2)).

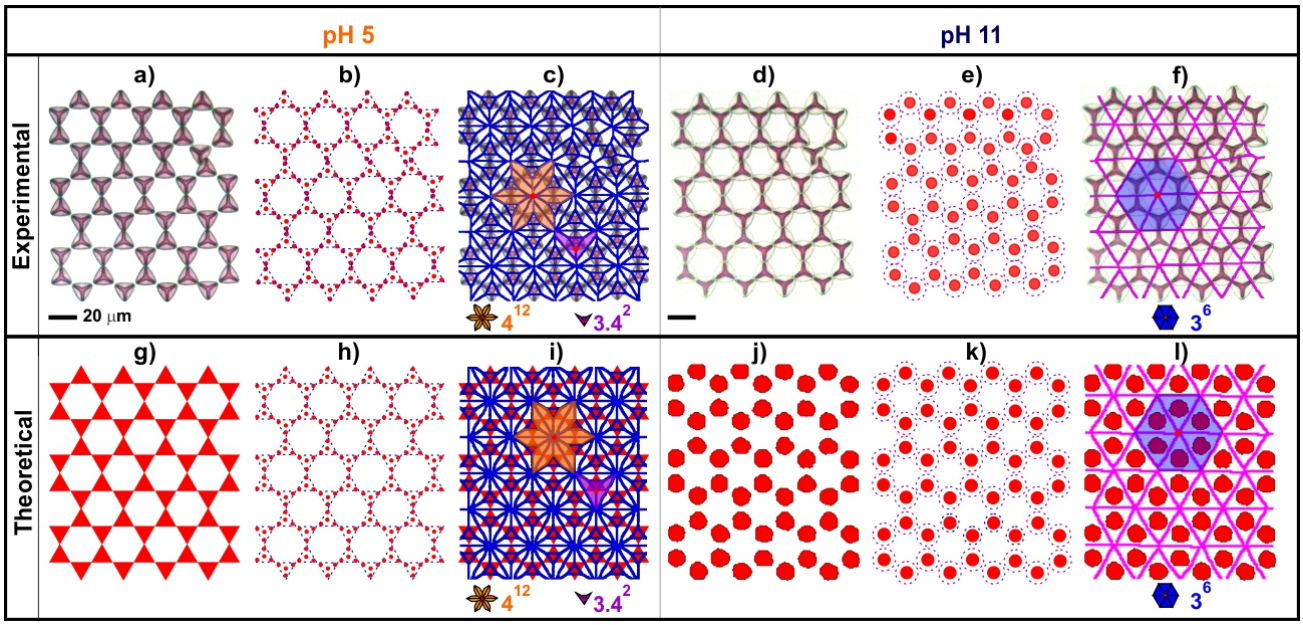

Figure S12. Transformation of 2D array with Kagome configuration. (**a**) Optical microscopic image of 2D array with Kagome configuration formed using geometrical shape-shifting BSA microstructures and (**b**) schematic outlining the shape contour of experimental BSA microstructures and their representative "nodes" to describe the reference point configurations. (**c**) Voronoi tesellation of 2D array with Kagome configuration superimposed with its optical microscopic image at pH 5. (**d**) Optical microscopic image of transformed array with hexagonal configuration formed using geometrical shape-shifting BSA microstructures and (**e**) schematic outlining the shape contour of experimental BSA microstructures and their representative "nodes" to describe the reference point configurations. (**f**) Voronoi tesellation of array with hexagonal configuration superimposed with its optical microscopic image, when pH increases from pH 5 to pH 11. (**g - i**) Array configurations, schematic outlining shape contour and reference points and the Voronoi overlays of theroetical Kagome array configuration, respectively. (**j - l**) Array configurations, schematic outlining shape contour and reference points and the Voronoi overlays of theroetical hexagonal array configuration, respectively.

Using the previously discussed "nodes" assignment to BSA microstructures (Figure S11), we demonstrate that the change in number of reference points as a result of triangle-to-circle shape-shifting of individual microstructures at pH 11, allow for both Kagome-to-hexagonal and open-

structured hexagonal-to-percolating hexagonal array transformations. First, we construct a 2D array with Kagome configuration by orienting triangular shape-shifting BSA microstructures outwards with corner-to-corner alignment in a periodic hexagonal manner, such that each triangular microstructure represents the three vertices of a triangle (Figure S12a).[11-13] The "nodes" are subsequently allocated at the vertices and center of individual microstructures to represent their D_{3h} symmetry. The resultant configuration (Figure S12b) of the reference points follows closely to theoretical illustrations employed in describing atomic/molecular structures of 2D materials with Kagome configuration. The observation is further supported by Voronoi tessellation of the experimental reference points (Figure S12c), which is in accordance to theoretical 2D array with Kagome configuration (Figure S12g–i) and consists of both characteristic vertex types of 3.4^2 (denotes a triangle and two trapezoid-shaped faces around a common vertex) and 4^{12} (denotes twelve trapezoid-shaped faces centered at a common vertex).

At pH 11, the BSA microstructures undergo rapid triangle-to-circle shape-shifting (Figure S12d), as evident from the fulfillment of our pre-defined criteria on protrusion index and area of occupancy. We assign a single "node" at the center of these shape-shifted circular BSA microstructures to denote its $D_{\infty h}$, and the resultant organization of "nodes" clearly depict a conventional hexagonal arrangement (Figure S12e). Voronoi tessellation of these "nodes" (Figure S12f) exhibits a vertex type of 3^6 (denotes six triangles around a common vertex), which can be indexed to the theoretical hexagonal array configuration (Figure S12j–l). The Voronoi tessellations of both arrays with Kagome and hexagonal configurations are in close agreement to their respective theoretical tessellations (Figure S12g–l). Such transformation of vertex types during the triangle-to-circle transformation of BSA microstructures as pH increases can be generally attributed to the reduction in reference points due to the loss of well-defined corners/vertices for the assignment of "nodes".

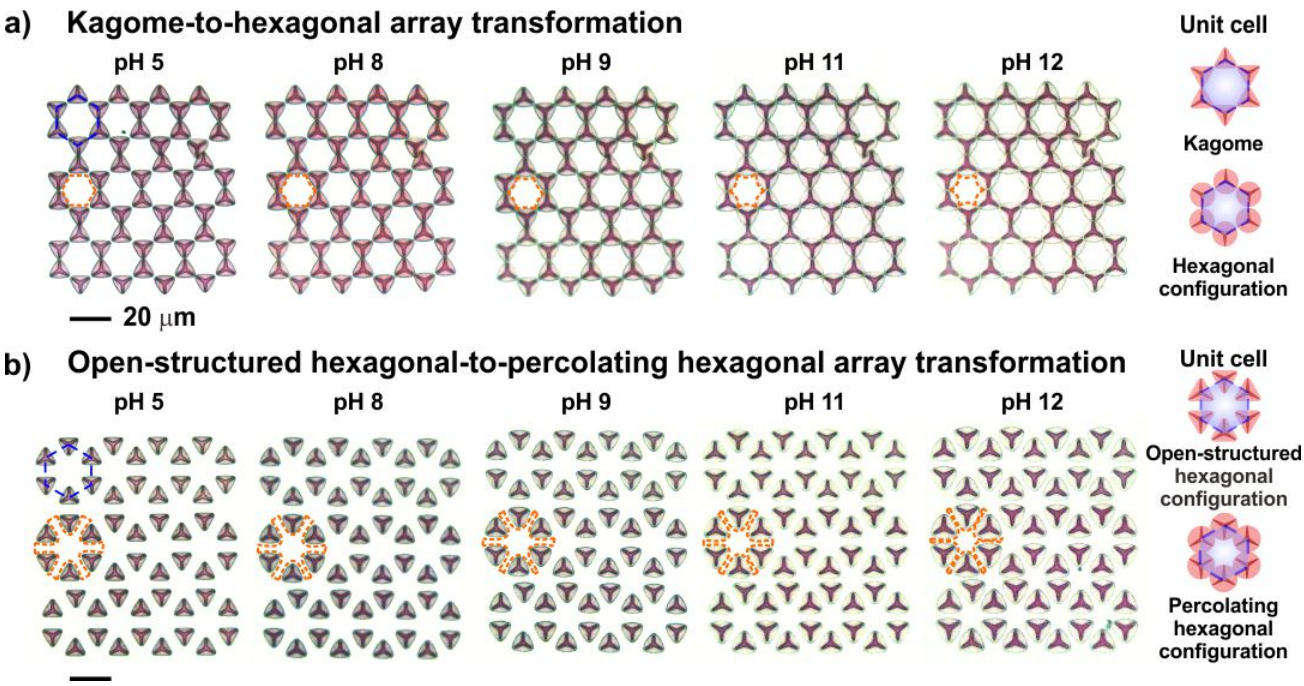

Figure S13. Transformation of array configurations at different pH. Optical microscopic images of arrays of geometrical shape-shifting BSA microstructures exhibiting (**a**) Kagome-to-hexagonal and (**b**) open-structured hexagonal-to-percolating hexagonal topographical transformations as pH increases gradually from pH 5 to pH 12, beyond the reversible pH range (pH 5 to pH 11) of BSA protein. Blue hexagonal contour represents a unit cell. Area outlined with yellow illustrates change in pore shape.

The calculated porosity decreases as pH is increased from pH 5 to pH 11, when both arrays with Kagome and open-structured hexagonal configurations transform into hexagonal configuration (Figure 5; Figure S13). The repeat unit of the arrays with Kagome, open-structured hexagonal and percolating hexagonal configurations is represented by hexagons as shown in Figure 5 and Figure S13.

Area of a hexagonal unit cell = $A_{\text{unit cell}}$

Area of BSA microstructures within a hexagonal unit cell at specific pH = $A_{\text{BSA, pH } X}$

Percentage of porosity = $[1- (A_{\text{BSA, pH } X} / A_{\text{unit cell}})] \times 100$

<u>Transformation of Kagome-to-hexagonal array configuration</u>

The calculation for percentage porosity at pH 5 and pH 11 (Figure S13) are demonstrated below:

At pH 5:

Using one hexagonal unit cell as an illustration:

Area of one unit cell = 583 μm^2 (quantified using ImageJ)

In a unit cell, there are six partial BSA microstructures that each has one-third of the original individual microstructure area. Since each BSA microstructure is determined to have an area of ~ 117.5 μm^2 using ImageJ,

Area occupied by BSA microstructures = $(6 \times \frac{1}{3} \times 117.5)\ \mu m^2$

$= 235\ \mu m^2$

Percentage porosity = $\left(1 - \frac{235}{583}\right) \times 100\ \%$

$= 60\ \%$

pH 12:

Using one hexagonal unit cell as an illustration:

Area of one unit cell = 583 μm^2 (quantified using ImageJ)

In a unit cell, there are six partial BSA microstructures that each has one-third of the original individual microstructure area. Since each BSA microstructure is determined to have an area of ~ 171.5 μm^2 using ImageJ,

Area occupied by BSA microstructures = $(6 \times \frac{1}{3} \times 171.5)\ \mu m^2$

$= 343\ \mu m^2$

Percentage porosity = $\left(1 - \frac{343}{583}\right) \times 100\ \%$

$= 41 \pm 3\ \%$

<u>Transformation of open-structured hexagonal-to-percolating hexagonal array configuration</u>

The calculation for percentage porosity at pH 5 and pH 11 (Figure S13) are demonstrated below:

At pH 5:

Using one hexagonal unit cell as an illustration:

Area of one unit cell = 699 μm^2 (quantified using ImageJ)

In a unit cell, there are six partial BSA microstructures that each has one-third of the original individual microstructure area. Since each BSA microstructure is determined to have an area of ~ 108.0 μm^2 using ImageJ,

Area occupied by BSA microstructures = $(6 \times \frac{1}{3} \times 108.0)\ \mu m^2$

$= 216\ \mu m^2$

Percentage porosity = $(1 - \frac{216}{699}) \times 100\ \%$

$= 69\ \%$

At pH 12:

Using one hexagonal unit cell as an illustration:

Area of one unit cell = 699 μm^2 (quantified using ImageJ)

In a unit cell, there are six partial BSA microstructures that each has one-third of the original individual microstructure area. Since each BSA microstructure is determined to have an area of ~ 216.5 μm^2 using ImageJ,

Area occupied by BSA microstructures = $(6 \times \frac{1}{3} \times 216.5)\ \mu m^2$

$= 433\ \mu m^2$

Percentage porosity = $(1 - \frac{433}{699}) \times 100\ \%$

$= 38\ \%$

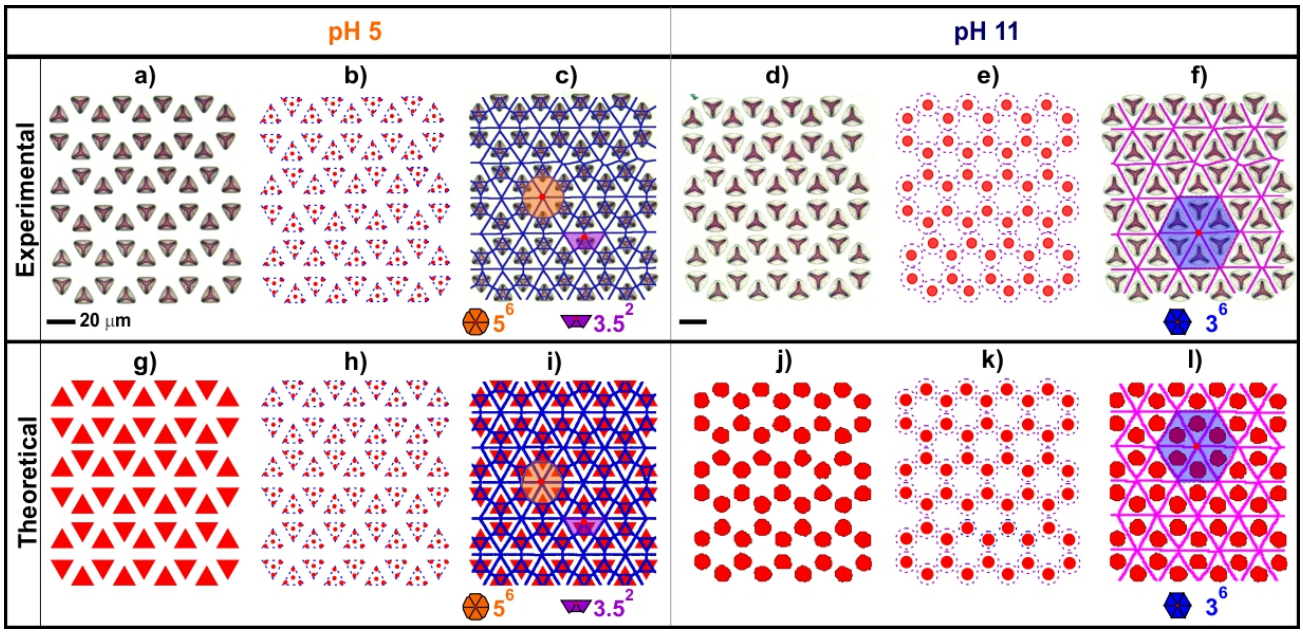

Figure S14. Transformation of 2D array with open-structured hexagonal configuration. (**a**) Optical microscopic image of an array with open-structured hexagonal configuration formed using geometrical shape-shifting BSA microstructures and (**b**) schematic outlining the shape contour of experimental BSA microstructures and their representative "nodes" to describe arrangements of the reference points. (**c**) Voronoi tesellation of array with open-structured hexagonal configuration superimposed with its optical microscopic image at pH 5. (**d**) Optical microscopic image of transformed array with percolating hexagonal configuration formed using geometrical shape-shifted BSA microstructures and (**e**) schematic outlining the shape contour of experimental BSA microstructures and their representative "nodes" to describe arrangements of the reference points. (**f**) Voronoi tesellation of transformed array with percolating hexagonal configuration superimposed with its optical microscopic image, when pH increases from pH 5 to pH 11. (**g - i**) Array configurations, schematic outlining shape contour and reference points and the Voronoi overlays of theroetical open-structured hexagonal array configuration, respectively. (**j - l**) Array configurations, schematic outlining shape contour and reference points and the Voronoi overlays of theroetical percolating hexagonal array configuration, respectively.

We fabricate pH-responsive and transformative 2D array with open-structured hexagonal

configuration by arranging inward oriented triangular shape-shifting BSA microstructures in a periodic hexagonal manner with edge-to-edge alignment, such that each triangular microstructure represents the three vertices of a triangle (Figure S14a). At pH 5, the array with open-structured hexagonal configuration consisting of individual triangular BSA microstructures exhibits vertex types of 3.5^2 (denotes a triangle and two diamond-shaped faces around a common vertice) and 5^6 (denotes six diamond-shaped faces centered at a common vertex) upon Voronoi tessellation of their "nodes" (Figure S14b,c). The array with open-structured hexagonal configuration rapidly transforms into percolating hexagonal configuration as the individual BSA microstructures undergo triangle-to-circle shape-shifting on exposure to pH 11 (Figure S14d). The change in array configurations from open-structured hexagonal configuration to percolating hexagonal configuration is again affirmed using Voronoi tessellation, where the latter exhibits a change of vertex type to 3^6 instead (Figure S14e,f) as number of reference points of each microstructure reduces from four to one during triangle-to-circle shape-shifting, which we verified to be in close agreement with their respective theoretical tessellation (Figure S14g–l).

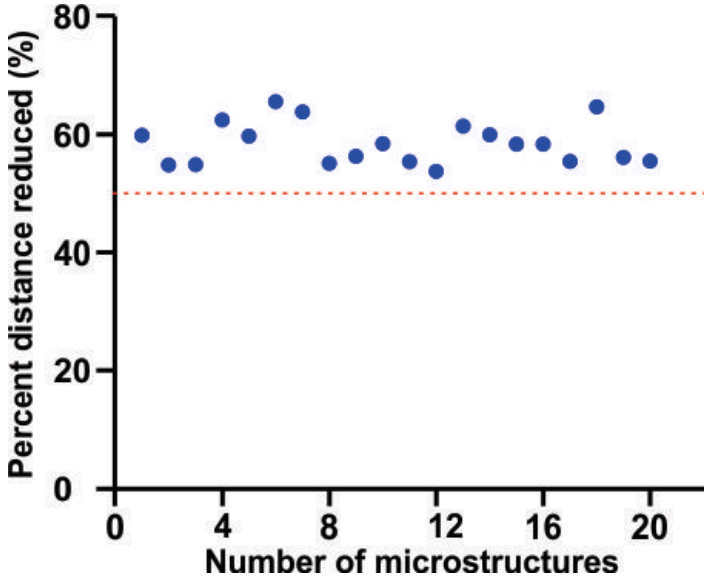

Figure S15. Change in neighboring distance. Graphs illustrating change in edge-to-edge distance between adjacent triangular BSA microstructures constructing an open-structured hexagonal array after transforming into a percolating hexagonal array at pH 11. Percentage of reduction in edge-to-edge distance is calculated by dividing difference in edge-to-edge distance before and after triangular-to-circle shape-shifting over edge-to-edge distance measured at pH 5. An array is considered to undergo topological transition due to change in physical connectivity when edge-to-edge distance decreases >50%. Transformation of open-structured hexagonal array configuration to percolating hexagonal array configuration is hence accompanied by topological transition as BSA microstructures have reduced edge-to-edge distance >50%.

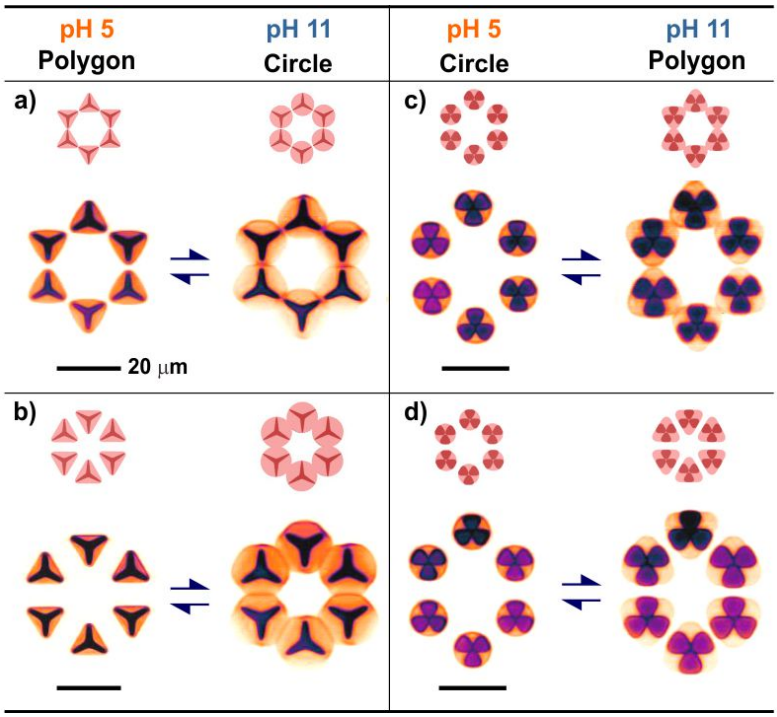

Figure S16. Unit cells of 2D array. Unit cells consisting of six individual geometrical shape-shifting BSA microstructures undergoing (**a**, **b**) triangle-to-circle and (**c**, **d**) circle-to-triangle transformations upon change in pH from pH 5 to pH 11. Schemes (top) and Raman images (bottom) illustrating change of (**a**) Kagome-to-hexagonal, (**b**) open-structured hexagonal-to-percolating hexagonal, (**c**) hexagonal-to-Kagome, and (**d**) hexagonal-to-open-structured hexagonal configurations.

To illustrate the capability of geometrical shape-shifting of BSA microstructures in constructing transformative 2D arrays, we arrange BSA microstructures into hexagonal unit cells representing Kagome (Figure S16a), open-structured hexagonal (Figure S16b) and hexagonal configurations (Figures S16c,d). For (a) and (b), the individual triangular BSA microstructures undergo shape-shifting to form circular microstructures upon the increase of pH 5 to pH 11. Consequently, the geometrical shape-shifting leads to the Kagome-to- hexagonal and open-structured hexagonal-to-percolating hexagonal transformation, respectively.

On the other hand, when pH increases from pH 5 to pH 11, we observe the circle-to-triangle shape-shifting of our individual BSA microstructures which results in the transformation of array

configuration from hexagonal configuration, to Kagome and open-structured hexagonal configurations (Figures S16c,d). Hence, our geometrical shape-shifting BSA microstructures and also their precise positioning/orientation are clearly essential for the construction of highly versatile transformative 2D patterned arrays.

SUPPORTING MOVIES

Supporting Information Movie 1. Dynamic circle-to-triangle shape-shifting of circular BSA microstructures embedded with three equally distributed triangle-shaped skeletal frames occurs when solution pH is changed from pH 5 to pH 11, and returned to initial pH 5.

Supporting Information Movie 2. Dynamic square-to-circle shape-shifting of BSA microstructures embedded with four equally distributed spike-shaped skeletal frames aligned along diagonal axes the square microstructures is demonstrated. Shape-shifting occurs upon solution pH is changed from pH 5 to pH 11, and returned to initial pH 5.

Supporting Information Movie 3. Dynamic circle-to-pentagon and circle-to-hexagon shape-shifting of BSA microstructures embedded with spike-shaped skeletal frames bound to corners of the polygons are shown. Shape-shifting is observed upon solution pH is changed from pH 5 to pH 11, and returned to initial pH 5.

Supporting Information Movie 4. Dynamic triangle-to-circle shape-shifting of BSA microstructures embedded with three equally distributed spike-shaped skeletal frames bound to corners of the triangular microstructures. Shape-shifting occurs in response to pH change from pH 5 to pH 11, and returned to initial pH 5.

Supporting Information Movie 5. Dynamic pentagon-to-circle shape-shifting of BSA microstructures embedded with five equally distributed spike-shaped skeletal frames bound to corners of the pentagonal microstructures. Shape-shifting is observed when pH is tuned from pH 5 to pH 11, and returned to initial pH 5.

Supporting Information Movie 6. Dynamic transformation of an array from initial Kagome configuration into distinct hexagonal configuration when solution pH is changed from pH 5 to pH 11.

Supporting Information Movie 7. Dynamic transformation of an array from initial open-structured hexagonal configuration into a percolating hexagonal configuration in response to change in pH from pH 5 to pH 11.

SUPPORTING REFERENCES

1. Lee, M. R.; Phang, I. Y.; Cui, Y.; Lee, Y. H.; Ling, X. Y. Shape-Shifting 3D Protein Microstructures with Programmable Directionality via Quantitative Nanoscale Stiffness Modulation. *Small* **2015,** *11*, 740-748.
2. Peters, T. J. Its Structure and Chemical Properties. In *All About Albumin: Biochemistry, Genetics, and Medical Application*, Academic Press, 1995; p 9.
3. Sun, H.-B.; Kawata, S. Two-Photon Photopolymerization and 3D Lithographic Microfabrication. In *NMR 3D Analysis Photopolymerization*, Springer-Verlag: Berlin Heidelberg, 2004; p 169-273.
4. Horizontal And Vertical Curves. In *Engineering Aid 1-Advanced Structural Engineering Guidebook*, Integrated Publishing, Inc.
5. Pollard, D. D.; Fletcher, R. C. Characterizing Structures Using Differential Geometry. In *Fundamentals of structural geology*, Cambridge University Press, 2005; p 86.
6. Marcombe, R.; Cai, S.; Hong, W.; Zhao, X.; Lapusta, Y.; Suo, Z. A Theory of Constrained Swelling of a pH-Sensitive Hydrogel. *Soft Matter* **2010,** *6*, 784-793.
7. Conway, J. H.; Burgiel, H.; Goodman-Strauss, C. *The Symmetries of Things*. A K Peters Ltd/CRC Press: Wellesley, 2008; Vol. 1.
8. Hahn, T.; Klapper, H. Point Groups and Crystal Classes. In *International Tables For Crystallography Volume A: Space-Group Symmetry*, International Union of Crystallography ed.; Hahn, T., Ed. Springer: Netherlands, 2006; p 785.
9. Kahr, B.; Shtukenberg, A. G. Histories of Crystallography by Shafranovskii and Schuh. In *Recent Advances in Crystallography*, Benedict, J. B., Ed. InTech: 2012.
10. Müller, U. Symmetry. In *Inorganic Structural Chemistry*, John Wiley & Sons Ltd: Chichester, 2007; p 12-29.
11. Rougemaille, N.; Montaigne, F.; Canals, B.; Duluard, A.; Lacour, D.; Hehn, M.; Belkhou, R.; Fruchart, O.; El Moussaoui, S.; Bendounan, A.; *et al*. Artificial Kagome Arrays of Nanomagnets: A Frozen Dipolar Spin Ice. *Phys. Rev. Lett.* **2011,** *106*, 057209.
12. Vedmedenko, E. *Competing Interactions and Pattern Formation in Nanoworld*. Wiley-VCH: Weinheim, 2007; Vol. 1, p 215.
13. Xie, S.-Y.; Li, X.-B.; Tian, W. Q.; Chen, N.-K.; Wang, Y.; Zhang, S.; Sun, H.-B. A Novel Two-Dimensional MgB_6 Crystal: Metal-Layer Stabilized Boron Kagome Lattice. *Phys. Chem. Chem. Phys.* **2015,** *17*, 1093-1098.